Electron concentration in the non-luminous part of the atmospheric pressure filamentary discharge

J Faltýnek[*] , **V Kudrle** , **M Šnírer** , **J Toman** and **O Jašek**

Department of Physical Electronics, Faculty of Science, Masaryk University Kotlarska 2, CZ-61137 Brno, Czech Republic

E-mail: faltynek@mail.muni.cz

CrossMark

Abstract

The non-luminous surroundings of atmospheric pressure plasma jets contain still substantial electron density which can be of practical importance, when e.g. reactant or precursor is introduced into this zone. Low signal-to-noise ratio makes the Stark broadening technique unsuitable there, and so we employed the microwave interferometry to determine the electron density during the plasma synthesis of graphene. The relatively long wavelength, tight geometry and the presence of overcritical plasma filament necessitated the use of a numerical solution of the Maxwell equations. Besides laying the groundwork of the method, the paper also discusses the importance of plasma density profile in the active filament and its surroundings. The results show that in radial distance ten times higher than a visually apparent plasma diameter, the plasma density was still around 10^{16}–10^{17} m^{-3}.

(Some figures may appear in colour only in the online journal)

1. Introduction

Microwave plasmas belong among the most widely used plasma sources in both science and industry due to simple design, good scalability and operation in a wide range of conditions. For example, atmospheric pressure microwave discharges are often used as excitation sources for analytical spectrochemistry [1], in gas reforming [2], for the destruction of harmful gaseous compounds [3], etc. Recently, microwave plasmas operated in atmospheric pressure argon have been used for the synthesis of advanced nanomaterials by admixing carefully selected precursor. As an example of great versatility, essentially the same apparatus was used to prepare well-oriented carbon nanotubes from methane [4], magnetic iron oxide nanoparticles from iron pentacarbonyl [5], and graphene from ethanol [6].

While other methods for nanomaterial production certainly exist and have their particular advantages, the plasma synthesis offers a unique combination of a simple, environmentally friendly, single-step process [7] producing high-quality product [8]. However, operating in a single-step regime brings a critical dependence on a delicate balance among many physico-chemical processes in the plasma. E.g. during the production of gas phase-synthesized graphene (GSG), the preferential [8] precursor is not simply a hydrocarbon, but an ether or alcohol, as they contain oxygen needed for proper nucleation. Detailed experimental and theoretical research of such plasmas is therefore of great importance.

Among many plasma parameters, the concentration of free electrons (i.e. plasma density) n_e is probably the most important. Interestingly, while the detailed model of atmospheric pressure microwave plasma in argon/ethanol mixture was recently published [9], it is not self-consistent and the electron density must be introduced from outside. Experimentally, these values have been provided based on Stark broadening

---

of H_α spectral line [10]. However, the accessibility of H_α line cannot always be guaranteed. E.g. in a practically desirable high production rate regime, a high precursor abundance is needed, which makes the H line(s) effectively obscured by massive molecular emission bands. Also, this method is not applicable if non-luminous part of the discharge should be studied. This is relevant when the precursor is introduced not directly with the main plasma gas, but separately (e.g. from the side) and so many important plasma-chemical processes take place on the plasma border. For these and other cases, an alternative method of plasma density measurement could be valuable.

For microwave atmospheric plasma torches/jets in general, the other suitable methods include high-pressure variant of Langmuir probe [11], Thomson scattering [12–14], active and passive optical diagnostics such as laser interferometry [15] or Stark broadening analysis of other significant spectral lines (e.g. Ar I, He I [16]), EM radiation [17] measurements, microwave interferometry or resonant cavity method.

Obviously, all of these approaches have varying theoretical, experimental and financial requirements, sensitivity, availability and other limitations. E.g. the electric probe method requires an advanced high-pressure sheath model and the probe itself is limited by the energy flow it can withstand (e.g. fly-through devices were attempted [18]). Similarly, the Thomson scattering experiment is not quite cheap and its sensitivity in atmospheric plasmas with large spatial gradients is noise limited [19] to higher electron concentrations, typically in the order 10^{18} m^{-3}. The Stark broadening always has a limitation of the spectral line discernibility, as discussed above. Microwave methods [20] are limited to plasma densities, which are still transparent to probing waves, need sufficiently homogeneous plasma and offer a very limited spatial resolution.

However, the recent advances in microwave technology (especially availability of coherent sources at THz frequencies) and computational power brought a renaissance of microwave techniques. Smaller wavelengths [21–23] give better spatial resolution and higher cut-off frequencies (i.e. the measured plasma density could be higher). This is important in atmospheric pressure discharges, which tend to have n_e quite high. Many authors, e.g. [24–26], successfully used microwave interferometry for atmospheric pressure plasmas diagnostics. The microwave methods are suitable [27–29] for studying the filamentary nature of atmospheric pressure plasmas and their (in)stabilities, too.

Computer modelling is a major part of this success as it can provide support and enhancement to experiment even where the classic, semi-analytic approaches and assumptions would fail. E.g. it seems possible to overcome (at least, in a limited fashion) a virtually fundamental problem of the cut-off frequency. Typical atmospheric pressure filamentary plasma [10, 30–32] with density 10^{20} m^{-3} would seem impenetrable to commonplace off-the-shelf microwave equipment operating in GHz or low tens of GHz. As the plasma is more-or-less opaque, the classical wave transmission problem becomes a wave scattering problem. Nevertheless, Maxwell equations remain valid

and can be numerically solved, giving a prediction of interferometrically observable amplitude and phase for a given geometry and complex plasma permittivity. Then going in reverse, using these pre-calculated tables from the EM field modelling, the experimentally observed quantities (amplitude and phase) can be converted to plasma permittivity and subsequently to plasma density. Moreover, based on numerical modelling one can discuss the influence of common experimental non-idealities, like misalignment of the interferometer, lateral offset of plasma filament, etc.

This paper tries to employ such numerically enhanced microwave interferometry, operating in K_a-band (around 34 GHz), for diagnostics of the darker area surrounding the active plasma filament, thus complementing standard measurements in the active plasma. The approach is principally similar to the one we used in our previous work [34]. However, in that paper, the plasma occupied a substantial part of (waveguide enclosed) beam cross-section, which effectively suppressed the scattering. Now, due to very different geometry of the current device, the probing beam can freely scatter off the active plasma column, which occupies only a very small part of the whole volume. The observed phase shift then should depend on the fine interplay between strong and localised scattering at filament edge, and propagation in much larger but much less dense surroundings.

While the paper is oriented towards the diagnostics of graphene producing plasma, to help understand our recent findings [33] of the relation between input power and graphene quality and quantity, its findings and conclusion should be useful to a more general audience.

2. Principles of selected methods of plasma density determination

2.1. Spectral line broadening

Optical emission spectroscopy (OES) is commonly used for non-invasive plasma diagnostics. When good resolution is available, the spectral line broadening can provide important information, e.g. about gas temperature or particle densities. As the contributions of various broadening mechanisms to spectral linewidth are different for each spectral line, some lines are more suitable for this task than others. Electron collision induced Stark broadening of H_α and H_β lines of hydrogen Balmer series is commonly used for electron density measurements in plasmas containing hydrogen [35–37].

Gigosos–Cardeñoso (GC) model [38] evaluates the Stark broadening (FWHM value) of H_β emission line as a function of n_e by a simple relation

$$\Delta\lambda_S = 4.8 \text{ nm} \cdot \left(\frac{n_e}{10^{23} \text{ m}^{-3}}\right)^{0.68116}. \quad (1)$$

However, other broadening mechanisms, such as instrumental, natural, Doppler and van der Waals broadening, must be taken into account to get correct Stark FWHMs from a measured spectral line profile [36]. During this, the deconvolution of the experimental Voigt profile into its Gaussian and Lorentzian parts is needed. Respective contributions of other mechanism

mentioned below were calculated and subtracted from experimental profile in a standard way [41, 42], leaving only the half-width corresponding to Stark broadening which was used for calculation of the electron density.

Random thermal movement of the radiating particle causes a Doppler shift, giving a Gaussian broadening profile with width [35]

$$\Delta\lambda_D = 7.16 \times 10^{-7} \lambda_0 \sqrt{\frac{T_g}{M}}, \qquad (2)$$

where λ_0 is the centre of the line, M is the ratio of atomic mass of the emitter and atomic mass unit m_u and T_g is gas temperature.

Impact pressure broadening by neutral particles (van der Waals broadening) has Lorentz profile with simplified width as calculated for Ar–H$_2$ mixture [35] at atmospheric pressure

$$\Delta\lambda_W = 5.521 \times 10^{-5} \text{ nm} \cdot \frac{p}{T_g^{7/10}} \quad \text{(Pa; K)}, \qquad (3)$$

where the T_g is gas temperature and p is pressure.

One can estimate T_g to be equal to a rotational temperature T_{rot} of molecular emission bands. In our case, the C$_2$ Swan system [40] was used.

Instrumental broadening, which has Gaussian profile, is independent of the plasma properties. It can be estimated by measuring spectral linewidth of the selected line close to H$_\beta$ under conditions when other broadening mechanisms are negligible [37]. In our case, a mercury calibration lamp is used and the broadened profile is approximated by the Gaussian with a FWHM of 0.024 nm because other broadening mechanisms are below 1 pm.

The natural broadening is commonly [37, 39] neglected due its low value, in order of 10^{-5} nm.

2.2. Microwave interferometry

The free electron density, n_e, influences the propagation speed of electromagnetic (EM) waves in plasma via the complex relative plasma permittivity ε_{pl}, which depends on probing frequency ω. Usually, the specific formula for plasma induced phase shift in microwave interferometry experiments is derived [20] under certain assumptions, which are normally taken as granted (infinite homogeneous plasma slab, perpendicular incidence transmission experiment, planar travelling wave only, Maxwellian EEDF, constant collision frequency, etc.)

However, real experiments are often rather far from these assumptions. In our case, the first three (geometric) assumptions above are not valid at all. Our plasma has a form of over-dense (over-critical) thin filament of active discharge, surrounded by a lower density (sub-critical) region. The probing wavelength is longer than the plasma filament diameter. The probed volume is in near-field [43] of the waveguides, i.e. the waves are non-planar, even non-TEM. Reflections, evanescent waves and scattering must be included. In effect, a full EM field solution is needed.

Fortunately, the two following assumptions about plasma properties are not so problematic. Ideally, the collision frequency ν_m should be independent of particle velocity, which

is also linked to the steady-state Maxwellian EEDF (electron energy distribution function). In real plasmas and high frequency approximation ($\omega \gg \nu_m$) the deviation from the ideal solution is rather negligible, even when the collision frequency depends on velocity and/or EEDF is non Maxwellian [44, 45]. Therefore, one can use the classical formula for the complex relative plasma permittivity

$$\varepsilon_{pl} = 1 - \frac{n_e e^2}{\varepsilon_0 m_e} \frac{\omega - i\nu_m}{\omega(\omega^2 + \nu_m^2)}, \qquad (4)$$

where e is the elementary charge, ε_0 is the permittivity of vacuum, m_e is the mass of the electron, ω is the angular frequency of probing microwaves and ν_m is the collision frequency for electron-neutral momentum transfer. In collision-less case, the simplified formula $\varepsilon_{pl} = 1 - \frac{n_e e^2}{\varepsilon_0 m_e \omega^2} = 1 - \frac{\omega_{pl}^2}{\omega^2}$ with ω_{pl} being the plasma frequency, directly suggests that for over-dense plasmas, plasma permittivity ε_{pl} would become negative and wave propagation would be impossible.

The more general formula (4) is relevant for both the transparent and over-dense plasma [46], which is crucial in our case. From the wave propagation point of view, one can thus formally describe the plasma as a dielectric (with complex refractive index $n_{pl} = \sqrt{\varepsilon_{r,pl}}$) even outside the common notion. The plot of such *analytic continuation* of the refractive index for a typical range of plasma parameters divided by angular frequency of the probing wave is plotted in figure 1.

Typical [47, 48] magnitude for ν_m for atmospheric pressure discharges is several 10^{10} s^{-1} up to a few 10^{11} s^{-1}, which means for our frequency 34.5 GHz that ν_m/ω will typically be around 0.1–0.5. While the high frequency assumption $\omega^2 \gg \nu_m^2$ would be better satisfied for even higher frequencies [49, 50], the squares in the inequality make these values acceptable.

As mentioned above, for dense plasmas, one must consider the wave scattering. With the probing wavelength similar to the scatterer dimensions, the Mie [51] formula exists as an analytic solution for several simple geometries. For our case, the 2D Mie scattering on a cylinder seems to be an obvious choice. Nevertheless, the analytical solution can not fully describe the experiment, as the incident waves are not necessarily planar, the plasma filament does not have exact boundaries, etc. Still, the results of the numerical EM model of scattering on a conductive cylinder in figure 2 are remarkably similar to analytic Mie predictions.

3. Experimental set-up

The 2.45 GHz atmospheric pressure coaxial plasma torch (for details of construction, see [52]) enclosed in metallic cylindrical reactor chamber (150 mm i.d., 400 mm height) is sustained in argon atmosphere with varying amount of the ethanol admixture (EtOH, C$_2$H$_5$OH).

The set-up (see figure 3) uses a vertical coaxial nozzle with two concentric gas channels—the central (0.8 mm diameter) for main argon gas (flow rate 700 sccm) and annular side channel (with inner diameter of 7.7 mm and outer diameter of 8.4 mm) for the admixture. This dual channel arrangement has certain advantages (especially stability) over direct
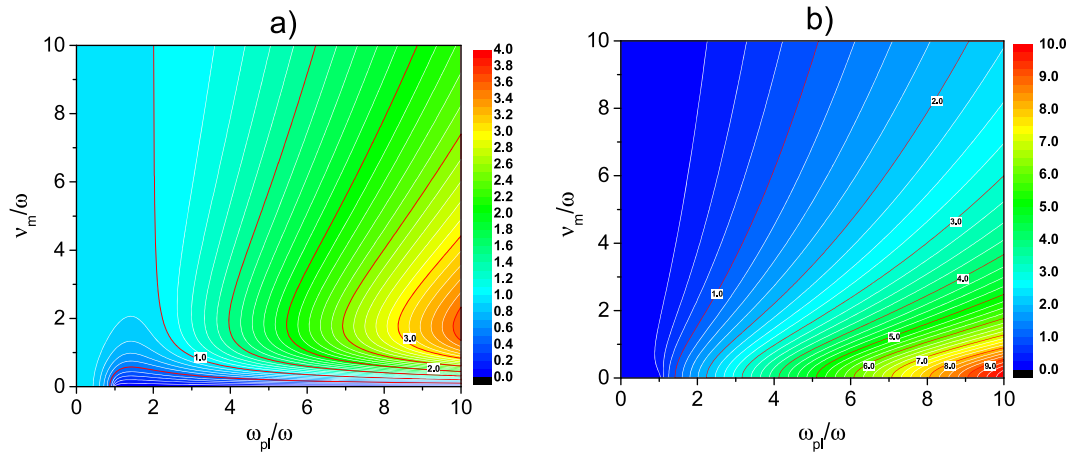
Figure 1. The real (a) and imaginary (b) part of the complex refractive index of plasma $n_{(pl)}$ as a function of a normalized plasma frequency ω_{pl} and collision frequency ν_m. The collision-less case can be seen at the bottom of the plot. Notice that due to collisions the real part of the refractive index is non-zero even in the classically overcritical region $\omega_{pl}/\omega > 1$ (and the propagating wave solution exists).
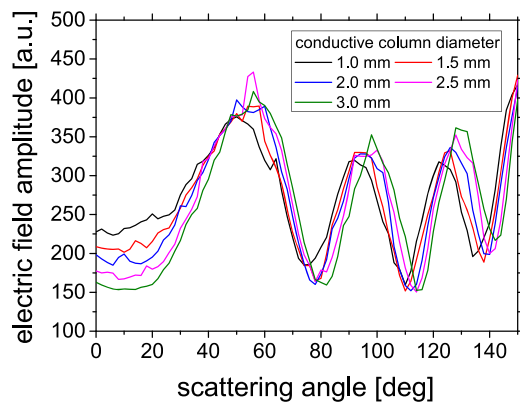

Figure 2. The numerically computed scattering pattern of the 34.5 GHz signal scattered off the 2D conductive column (polarization aligned with the z-axis of the column).

pre-mixing, used e.g. in axially injected torch TIA [53]. The ethanol vapours are carried by auxiliary argon passing through a bubbler containing liquid ethanol. Their amount was controlled by this auxiliary argon flow rate. By gravimetry, the empiric ratio of 1 sccm of ethanol per 100 sccm of auxiliary argon was found. The exhaust gases exit the reactor through the upper flange and extended tubing to prevent back streaming of air.

The investigated parameters are the driving power (20–120 W) and the flow rate of the auxiliary argon carrying admixture (typically varied between 0 sccm and 40 sccm).

For the microwave diagnostics, the Mach–Zehnder configuration of 34.5 GHz (K_a band, WR28 waveguide) interferometer (with its probing arm extending inside the reactor chamber) is used. The MW signal is produced by a Gunn diode oscillator (GKa-350, Spacek Labs Inc.) The frequency of the source is stabilised by the resonant cavity, with a vendor specified thermal stability in the order of $100\,\text{kHz}\,\text{K}^{-1}$. The passive components of the interferometer (attenuator, phase shifter, isolator, waveguide parts) are standard quality, off-the-shelf MW equipment. Signals from the probing and reference arm are

eventually combined in the magic tee and two detectors (diodes, DKa-2N, Spacek Labs Inc.). Actually, the correct calibration of these detectors (beyond manufacturer provided datasheets) is quite important. This is due to the nature of equation (5) (subtraction of close numbers) where the imprecise conversion between power and voltage can, very easily, lead to incorrect results. This interferometric set-up is noteworthy for the close proximity of probing arm waveguides to the plasma without any dielectric barrier in between. This was necessary for continuous operation during graphene plasma synthesis, where the high temperature and powdery deposit would be detrimental to any window material. Gas sealing of the waveguides was made at their upper flanges using thin PTFE foil. The whole set-up demanded careful shielding, as any stray signal at the power frequency (2.45 GHz) would be rectified by K_a band detectors, distorting the measurement.

Using calibrated detectors, the relative phase ϕ between the probing and reference arms can be determined [43] from the powers P_1 and P_2 incident on the detectors 1 and 2 via the magic-tee (i.e. 180° hybrid) coupler equation

$$\cos^2(\phi) = \frac{(P_1 - P_2)^2}{4(P_1 + P_2)|_{ref=0}[(P_1 + P_2) - (P_1 + P_2)|_{ref=0}]},$$
(5)

where the $|_{ref=0}$ labeled parentheses correspond to measurement with fully attenuated reference arm of the interferometer. This means that an actual determination of phase consists of two measurements—one, when the reference arm is attenuated and second, when there is some defined power going through. In this (quadrature) way the changes in phase can be separated from changes in amplitude. Practically, phase differences around 1° can be distinguished, anything below that is within the experimental error range.

OES was carried out through the fused silica windows in the reactor walls to study the dependence of selected plasma parameters on experimental conditions and spatial position. Overview spectra in 200–1000 nm range were recorded using Avantes ULS3648TEC spectrometer equipped with fixed $300\,\text{gr}\,\text{mm}^{-1}$ grating and resolution of 1.4 nm. The signal was
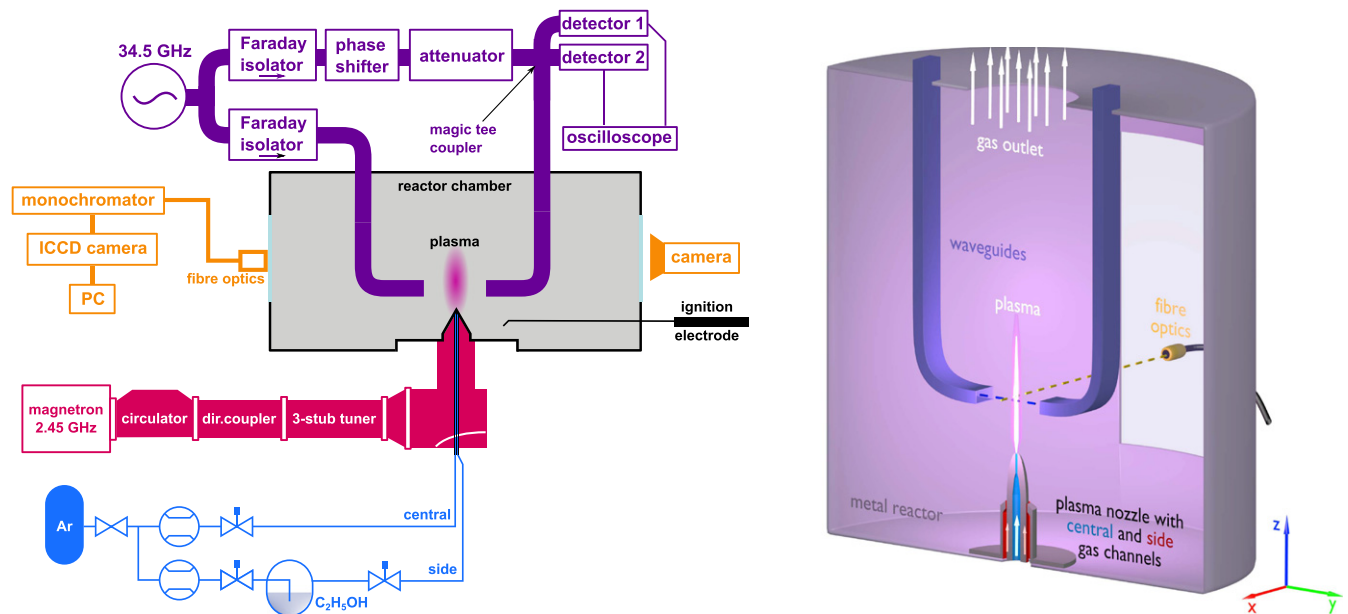
Figure 3. Left: the schematic drawing of the experiment—microwave torch together with OES and microwave interferometry diagnostics. Right: the 3D cross-section of the reactor, which depicts the actual geometric arrangement.

collected from the whole discharge by placing optical fibre at a distance of 30 cm. The overview spectra were mainly used for real-time monitoring of discharge conditions.

Higher resolution spectra needed for temperature (from the molecular rotational structure) and electron density (from H_β Stark broadening) determination were recorded using Andor Shamrock 750 mm spectrometer (2400 gr mm^{-1} grating and resolution of 0.02 nm) equipped with Andor Newton CCD DU940P-BU2 detector. The optical system used fused silica aspherical lens ($f = 15$ cm) to magnify the plasma for spatially resolved measurements. Optical fibre was placed in the plane of projection, mounted in the manually adjustable linear 2-axis translation stage.

Finally, the Nikon D5200 camera equipped with Nikkor 200 mm lens, is used to capture the brightness (emission) profiles and monitoring snapshots (mainly alignment of the waveguides). It was possible to image the plasma either from the side or from the top.

4. Numerical model of microwave interferometry

Most laboratory atmospheric pressure discharges are contracted with filament diameter in mm or even sub-mm range. This is much smaller than the wavelength and the beam width of a typical X-band or K-band microwave interferometers. Moreover, their dense plasma (around 10^{21} m^{-3}) is overcritical and thus opaque for such interferometers [54–56]. That is, indeed, also our case with plasma diameter approx. 1 mm, beam width 7 mm, plasma frequency around 2×10^{12} s^{-1} and probing frequency 2×10^{11} s^{-1}. Fortunately, the numerical solution of Maxwell equations inherently includes all wave phenomena (reflection, total reflection, refraction, scattering, diffraction, etc.)

In our previous paper [34], the probing EM field was tightly constrained inside the metallic waveguide (plasma filament passing through a hole in the wall), and therefore the angular scattering or refraction on spatial inhomogeneity did not manifest much. In the open space (or large experimental device), however, it is theoretically possible for a part of the wave to avoid (go around) the plasma filament along a longer path and still reach an opening of the second waveguide, contributing to the final measured phase. This potentially makes the phase more sensitive to small geometry variations (see e.g. angular interference pattern of Mie scattering in figure 2). As a consequence, the model needs a rather fine meshing to give reliable results.

As before, we have chosen the COMSOL Multiphysics software and its radiofrequency (RF) module suitable for computation of high frequency EM wave interaction with matter. The user defined model geometry is divided into subdomains (e.g. plasma region, air, conducting walls, etc) that are characterized by a set of material constants (permittivity, permeability, conductivity). The Maxwell equations are then numerically solved on the full domain with given boundary conditions. The solver is general enough that even overcritical plasma with negative permittivity is allowed.

The *frequency domain study* models the two waveguide sections (with input and output port, rectangular TE$_{10}$ mode) facing each other with the cylindrical plasma domain in between. The most careful approach would be an inclusion of full reactor geometry with all details such as the electrode shape, flanges, windows, etc. The downside of this approach is the large volume of the reactor. Respecting the general necessity of computation to have a sufficiently dense mesh (several elements per wavelength and across any subdomain) and using the 34.5 GHz signal (free-space wavelength approx. 8 mm),
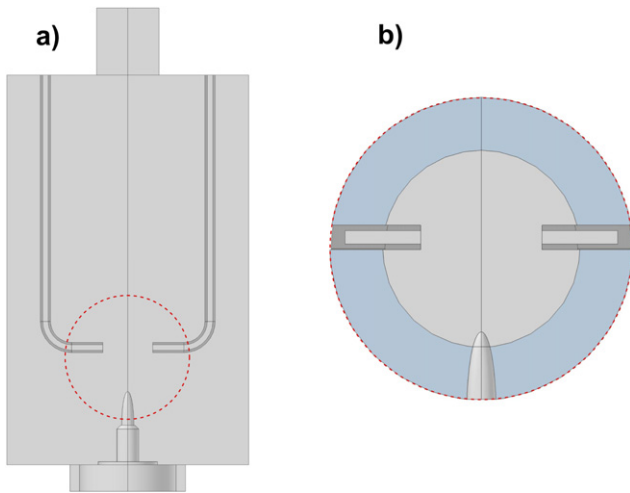
Figure 4. The (a) full-size model geometry and (b) the geometry of the cropped model with PML (blue tint).

this full 3D model (see figure 4(a)) would inevitably have extreme memory and CPU demands.

Combined with the necessity of performing parametric and prototyping studies, this is not a viable solution. Reduction to a cylindrical 2D model is tempting but impossible, as the interferometer waveguides break the angular symmetry. Since the choice of solver algorithm or adjustment of the mesh topology have a marginal impact in the majority of cases, the only optimisation with significant impact is the cropping of the full reactor volume to the area closely surrounding the waveguides and plasma. Then, the model can be reduced (see figure 4(b)) down to a much smaller sphere encompassing only the plasma interaction region between the waveguides. The outer border of this sphere is formed by the perfectly matched layers (PML), which as perfect absorbers, effectively enforce the Sommerfeld radiation boundary condition.

While the advantages of this cropped model are evident (substantially reduced mesh size, lower complexity of the model, improved performance), the question of validity naturally arises. Fortunately, both modelling and experimental results suggest (see figure 5) that the measured interferometric phase is substantially influenced only by the area situated in the line of sight between the two opposing waveguide openings. The remaining question of possible multiple wave reflections at the conductive reactor walls was analysed numerically as well, with the result that they can be safely neglected. This simplification is therefore justified.

All relevant geometric parameters of the model are defined as 'variables' and can be parametrically swept (waveguides mutual position, plasma filament position, length, thickness) to cover a range of experimental situations.

During the model development process, various scenarios and set-ups (as there are many free parameters) were prototyped. In the first approximation (model A), which does not consider the radial profile of electron concentration, the plasma domain is a thin homogeneous column homogeneously filled by 'plasma material' with complex permittivity according to (4). Remaining volume is filled by air (i.e. material with $\varepsilon_r = 1 + 0i$).

The advanced models B and C (see below) generalise the plasma material to be radially inhomogeneous. This corresponds to reality—high electron density inside the active plasma region, which drops appropriately outside of it. The introduction of inhomogeneity necessitates adding dense concentric mesh layers with progressively decreasing plasma density.

While it was found that some model parameters are not crucial (the outcome is mostly insensitive to them, at least in range of their typically expected values), the significance of the above-mentioned radial profile (especially outside the dense plasma column) was particularly revealing.

5. Results and discussion

A freely expanding microwave plasma torch (as many other atmospheric pressure jets) produces a plasma with a typical flame-like visual structure consisting of two regions [10, 53]: high intensity dart tipped by more diffuse plasma plume formed usually by molecular emissions of admixture—air, water vapours, precursor residuals, etc. While these admixtures may be unwanted (impurities), they are still very useful for optical diagnostics, as they provide spectral features needed as probes for temperature (OH, N_2, N_2^+, etc) or electron density measurements (H).

If the argon discharge is enclosed in a reactor vessel, these impurities are significantly suppressed, leading to a different plasma structure. E.g. in [57], bright axially elongated filament(s) surrounded by low intensity plasma halo/shell was reported. The low abundance of emitting species needed for temperature and electron density measurements requires supplying them in defined quantity on purpose, typically in the form of hydrogen gas or water vapour [58–60].

In our experiments, however, only the filament (i.e. no halo/shell) was observed and no further diagnostic admixtures were needed as we studied the plasma torch during graphene synthesis from ethanol. Therefore, hydrogen, oxygen and carbon are present as a result of ethanol decomposition in plasma and H_β emission line can be used for electron density measurements. Molecular emission spectra of C_2 Swan system were used for gas temperature estimation [40] via state by state fitting using MassiveOES software [61–63].

For the studied range of admixture flow rates, the overall changes in plasma appearance and structure were relatively small (except a partial retraction of the filament), which is important for the validity of numerical model predictions. An illustrative photograph of the discharge is shown in figure 6. The length of the discharge was somewhat impaired by the proximity of metallic interferometer waveguides, yet the thickness and emission characteristics of the filament appear, fortunately, much less sensitive to their presence. Generally, we operated in a range of conditions where the filament was mostly stable and straight. The position and shape of the filament remained typically stable for several minutes. Moreover, the time averaging of interferometric data was used to suppress any residual stochastic stray movements of the filament.

Analysis of hydrogen emission lines permits us to estimate (line of sight averaged) electron density and its axial and lateral
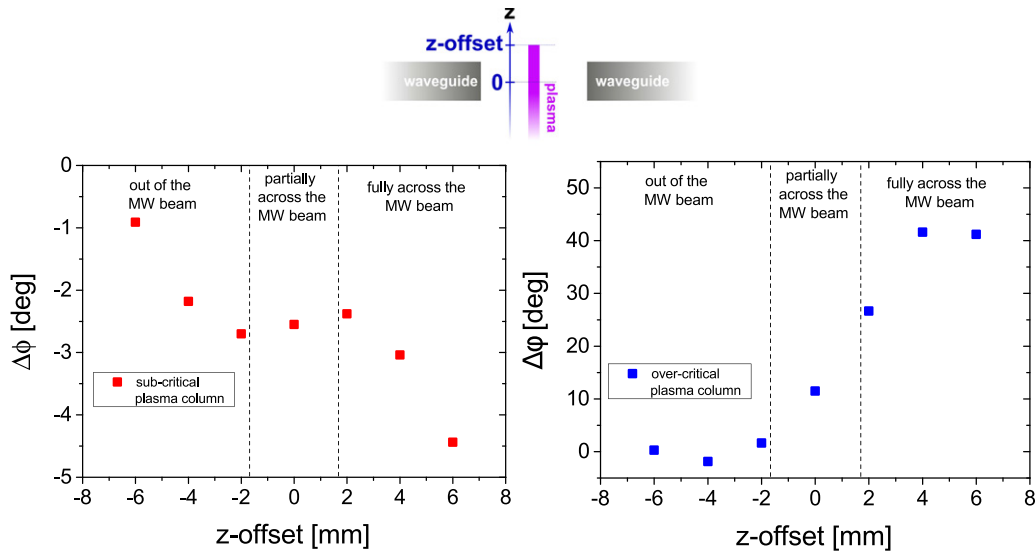
Figure 5. The comparison of the calculated plasma induced phase shift as a function of the plasma filament *z*-offset (axial, see the top schematic illustration for reference) from the waveguide line of sight for both sub-critical (left) and over-critical (right) plasma column. The vertical dashed lines correspond to waveguide edge positions. For demonstration purposes, the 2 mm column thickness results are shown.
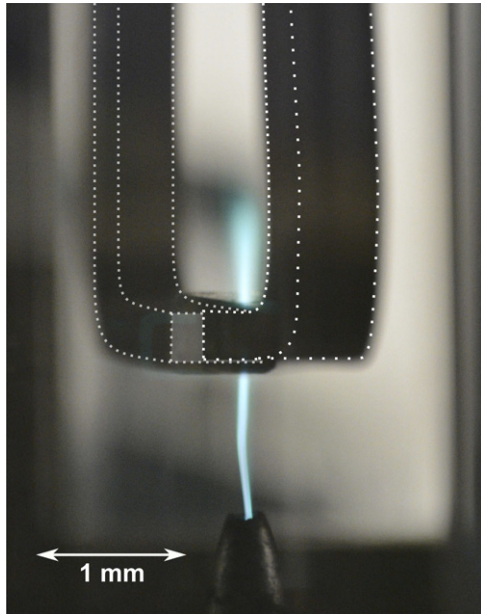

Figure 6. Illustrative photography of the nozzle, filament and waveguides configuration. For better clarity, the waveguide edges are artificially highlighted. Here, the conditions are 700 sccm Ar, 50 sccm Ar + 1% EtOH, 90 W.

distribution in the active filament. However, these optical measurements are limited by a low emission intensity in the filament surrounding and by limits of Stark broadening theory for low electron concentrations [38]. In contrast, the microwave interferometry is able to provide results even in this dark, low density region due to its line integrating properties over longer paths.

As it turns out, such an experiment indeed produces measurable and repeatable negative phase shifts (e.g. approx. 15° for 50 W driving power, 700 sccm pure Ar flow). One cannot

intuitively deduct which portion of this phase shift should be attributed to the central filament and which to its less dense, but more extended surroundings. A numerical study is therefore needed.

The goal of the EM field modelling is to calculate the phase shift for a given set of parameters. When such phase shifts are pre-calculated for a range of parameters, a reverse process (fitting) can be used to extract the value of an unknown parameter from experimentally observed phase shift.

As it turned out, for the collision frequency in the expected range (approx. 10^{10} s^{-1} to 10^{11} s^{-1} for these discharges [47, 48]), its influence on calculated phase shifts is fortunately rather low. Therefore in further text (models A through C) the results are presented for the rough estimate $\nu_{\mathrm{m}} = 5 \times 10^{10}$ s^{-1}.

5.1. Model A — homogeneous plasma filament

In the simplest model A (homogeneous dense plasma filament, no plasma surroundings), the only variable parameters are the filament diameter and its plasma density (geometry of the reactor and the interferometer being fixed). A typical pattern of the resulting EM field is shown in figure 7.

For a rather crude model A, the rough estimation of diameter ($2r = 0.7$ mm) as experimentally observed FWHM of light emission lateral intensity profile can be considered sufficient. The model then provides figure 8, a dependence of phase shift on filament plasma density. Perhaps unsurprisingly (as the plasma is dense and the interaction region is very small), the graph shows that, across several orders of magnitude of n_{e}, the predicted phase shifts are below the instrumental error (which is approx. 1°), exceeding this threshold only for very high plasma densities.

While the absolute value would seem to approach experimentally observed phase shifts at extremely high plasma densities, the sign of these phase shifts is wrong. Moreover, such densities are usually only observed immediately at the plasma
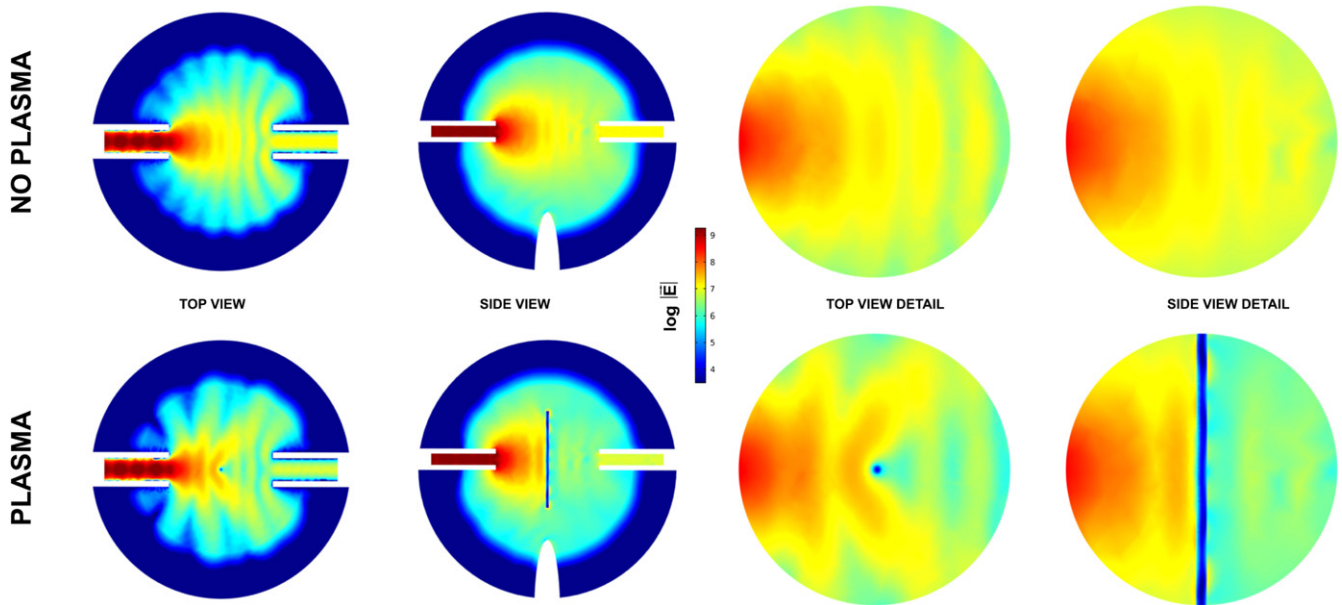
Figure 7. A typical top- and side-view of the computed EM field. Colour coded electric field norm $|\vec{E}|$ in empty resonator (upper row) and in presence of the dense plasma filament (lower row, plasma column outline added). Note the angular scattering (plasma, top view detail) with maximum around $55°$, corresponding very well with analytic predictions in figure 2.
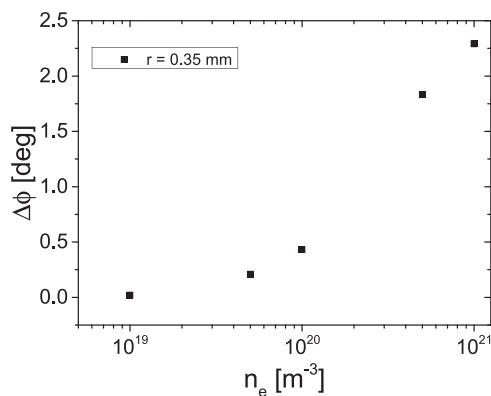

Figure 8. The computed phase shifts, when only the homogeneous plasma filament core contribution is assumed—model A (oversimplified, see text).

nozzle [36], not farther downstream. The results of the model A are therefore dubious at best.

In order to assess them further, the Stark broadening measurement was conducted (as explained above, hydrogen atoms were present due to decomposition of ethanol admixture). At low flowrates of precursor (0–0.5 sccm EtOH) the H_β line was dominant compared to the molecular Swan C_2 band nearby and their overlapping was negligible. Therefore, H_β could be easily used for electron density estimation. Results are in agreement with previous measurements on the same experimental set-up and theoretical model made by [36]. The plasma density was approximately $n_e \sim 10^{21}$ m^{-3} at the tip of the nozzle. At position 15 mm downstream, where the waveguides are placed, the GC model [38] would yield approximately $n_e \sim 2 \times 10^{19}$ m^{-3}. While majority of the broadening models were intended for electron densities above 10^{20} m^{-3} [38, 64, 65] it was shown

[66] that the GC model can be used above 4×10^{19} m^{-3} for H_β. Below this density, the fine structure should be introduced. As it was not included in our measurement and therefore, n_e value is underestimated [37]. However, even this underestimated value is higher than the critical density for 34.5 GHz signal, and so the scattering of the probing microwave beam on the plasma filament is truly important.

The wrong sign of the phase as calculated by the homogeneous model A means that the inhomogeneous model B (which also includes the regions with subcritical plasma) is absolutely necessary.

5.2. Introducing the radial profile of electron concentration—model B

A determination of the radial profile of plasma density in atmospheric pressure plasma jet can actually turn out quite challenging, both experimentally or theoretically. It is due to large gradients, existence of instabilities and generally insufficient understanding of physics and dynamics of the filamentary plasmas (qualitative or particular so far) [29, 67–69]. Unfortunately, as the probing microwave beam is relatively large, the interferometer itself cannot be used to perform laterally resolved measurements and extract the radial profile (although there are some pioneering attempts to do so [70]). Therefore some other means of profile determination are necessary.

Naively, the easiest option is relating the profile of electron density to that of relative light emission intensity. However, it is clear that the relation between excited species and electron densities is not simple, at least due to the role of electron energy distribution function, which is *a priori* unknown. The second option is to rely on established methods such as Stark broadening, Thomson scattering, etc. Finally, a fully self-consistent plasma model could be theoretically developed,
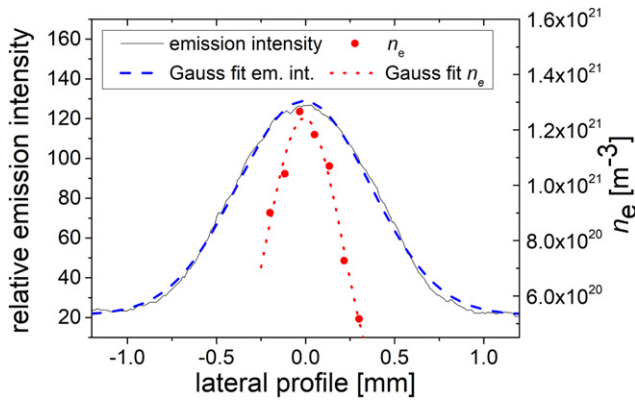
Figure 9. Lateral profile of the electron density n_e from Stark broadening and the light emissions (from imaging in VIS range) of a plasma filament. (700 sccm Ar, 40 sccm Ar + 1% EtOH, 60 W, 5 mm from nozzle exit).

but the inclusion of all the peculiarities (e.g. column constriction, instabilities, etc) of the atmospheric pressure filamentary discharges is generally still beyond state of the art in plasma modelling.

Stark broadening is an obvious choice for spatial profiling, as it was done and discussed before by many investigators, e.g. [30, 36, 37]. It should be noted that problems mentioned in section 5.1 for averaged plasma density are even worse for its spatial profiling, as the n_e radially decreases and so gets easily out of GC model validity range. In combination with generally lower intensity of H_β emission farther from the axis, the dependable results are limited only to the central region of the filament, not permitting to profile outer region of the filament and especially not the filament surroundings. Assuming that the profile (at least its shape) remains roughly the same along the plasma column, one can carry out the measurement closer to the nozzle, where the electron density is sufficient and the GC model remains appropriate. As an example, a typical lateral electron density profile and light emission profile covering the centre of the filament is shown in figure 9 for axial position 5 mm (i.e. much closer to the nozzle than the position 15 mm of microwave interferometry measurements).

The light emission profile nicely follows the Gauss curve. For electrons, the interpretation is more questionable, as the shoulders of the spatial profile are experimentally inaccessible. Fortunately, among papers investigating the spatially resolved electron density of atmospheric jet filament, one [31] was measured directly on our experimental device at similar experimental conditions using Thomson scattering. This method is considered superior as it can yield more precise results with decent spatial resolution and lower sensitivity limit. Their published colour maps can be recalculated back to actual profiles, shown in figure 10.

The bulk of the filament (consider the logarithmic n_e scale) is well described by the Gauss curve, also in agreement with [30]. However, farther from the axis, there is a noticeable deviation from the Gauss curve as the plasma density decrease is slowed down. Also, the data from a self-consistent model, recently developed for free-expanding surfatron discharge simulation [71] suggests that this effect is real and

not some unreliability of Thomson scattering for low electron concentrations.

Nevertheless, as the bulk of filament is Gaussian, the model B considers only this analytic shape and ignores any 'slowing down'. The spatial distribution of n_e for varying radius r is therefore parametrised as

$$f_{\mathrm{Gauss}}(n_{e,c}, G) = n_{e,c} \cdot e^{-(r)^2/G}, \tag{6}$$

where $n_{e,c}$ (abbrev. for centre) is the central (peak) value of the electron concentration and parameter G controls the width. A series of numerical simulations was run, for several values of G around the value estimated from experimentally observed filament half-widths. The results of these simulations are shown in figure 11.

Compared to model A, there is some improvement of sensitivity, which has to be attributed to the shoulders of the spatial distribution. Significantly, the interferometric phase shifts according to the model B can be either positive or negative. This depends on which process (the scattering on the over-critical part or the propagation in sub-critical part) dominates. More specifically, during model prototyping and iterating, it became apparent that: (i) the mechanism of over-critical and sub-critical plasma region contributions may be as simple as shown in figure 12 and (ii) the positive contribution of the over-critical central part of the filament is often (smaller radii, lower $n_{e,c}$) insignificant. It follows that, in our case, the Gauss function width parameter is not critical and can be safely estimated to be equal to e.g. that from light emission without introducing a significant error.

Yet again, these numerical results do not reach the experimentally observed phase shifts ($<-10°$).

5.3. Two part profile function—compound model C

Unsatisfactory results of the previous models A and B (as compared to the experimentally observed phase shifts) suggest the existence of extended shoulders of the electron concentration spatial profile. It should be noted that despite much lower electron density than in the central maximum, these shoulders may still play a globally significant role in transport and electron collision processes purely due to geometrical volume factor (scaling with r^2).

The Gauss function (while satisfactory for the active filament itself) has shoulders decreasing too fast. However, as it was remarked earlier, during the discussion of figure 10, the reference data indeed hinted on a composed spatial distribution—Gaussian in central bulk and some slower decreasing function in its surroundings. Therefore, the model C includes both these components. Since the results of previous models suggest that interferometric phase shifts are rather insensitive to the innards of the dense plasma filament, many parameters (degrees of freedom) of the model can be fixed, simplifying the modelling and subsequent analysis greatly. More specifically, while the filament presence is critical for the scattering and must be included, the exact width of the filament is not.

The task is then mostly reduced to choosing the appropriate function for the electron concentration profile outside the active plasma region. While the class of possible
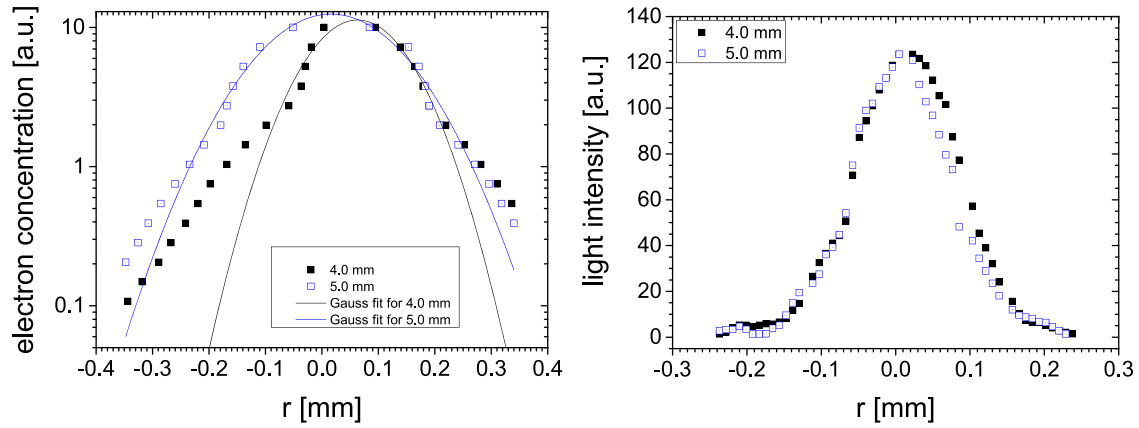
Figure 10. Radial profiles extracted from colour maps in [31]; left—electron density from Thomson scattering and right—light emission at axial positions 4 mm and 5 mm downstream from the nozzle. Electron density profiles are fitted by Gauss curves.
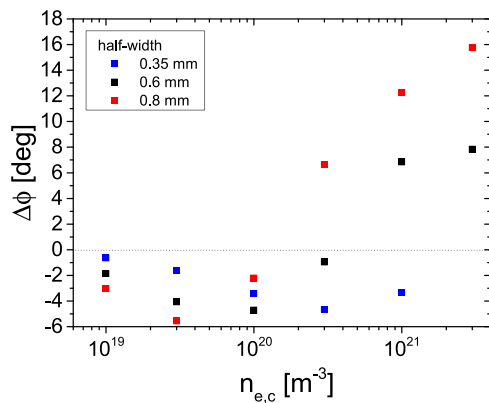

Figure 11. The model B (Gauss profile of n_e computed phase shifts for several filament half-widths (HW = $\sqrt{G \ln(2)}$).
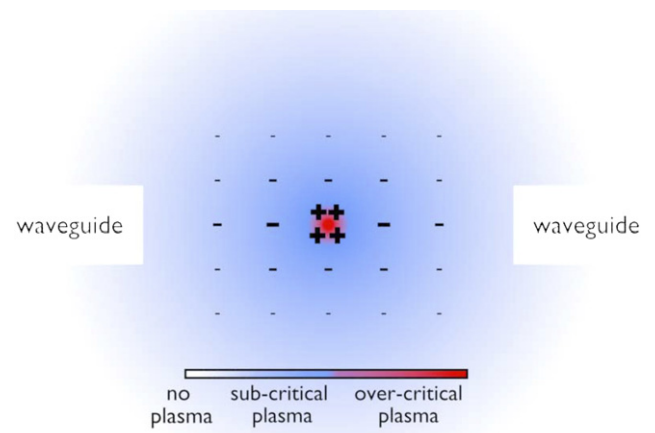

Figure 12. The deduced diagram of contribution to the EM wave output phase from different plasma regions. The size of plus/minus signs represents the magnitude of the effect, while the colour represents the relative electron concentration. The over-critical region acts mostly as an obstacle, prolonging the wave path and increasing the output phase. In contrast, in the sub-critical region the EM wave propagates in the most common way, only with the phase velocity larger than in vacuum, leading to a negative phase shift contribution.

functions is infinite, we can at least fix its most general properties—it should be continuous, monotonously decreasing and have boundary conditions (it should fall towards zero on the outer boundary, it should have a continuous transition from the Gauss function on the inner radius). Physics, practicality and even certain aesthetics prefer that this function should be 'reasonable'.

The experimental viewpoint is that linearly decreasing shoulders in semilogarithmic plot (figure 10, left) suggest that a simple exponential function (7) could be a suitable candidate. The theoretical viewpoint is that solution of the diffusion equation in cylindrical coordinates is a first order Bessel function (8). We *a priori* do not know the correct spatial distribution function, but these two candidates are actually quite representative. The exponential is rather fast decreasing, giving prominence to the region in close vicinity of the Gaussian active filament, while the Bessel function is quite flat and so, due to the volumetric r^2 factor, it effectively accentuates regions farther off-axis.

Among many (again, infinitely many) possibilities of gradual transition near filament edge, we chose to do it by simple stitching the central Gaussian and the outer distribution function together at a certain radius r_0 from the centre. So, for $r \leqslant r_0$ the spatial distribution is Gaussian (6), while for $r > r_0$

the profile is exponential or Bessel

$$f_{\exp}(n_{e,s}, F) = n_{e,s} \cdot e^{-(r-r_0)/F} \tag{7}$$

$$f_{\mathrm{Bes}}(n_{e,s}, R) = n_{e,s} \cdot J_0(2.405(r-r_0)/R). \tag{8}$$

The main parameter of both profiles is the electron concentration $n_{e,s}$ at radius $r = r_0$, where they are stitched to the central Gauss profile. The second parameter for Bessel profile (8) is its radius (first zero) R. The second parameter for the exponential profile (7) is its characteristic length F. An initial guess of $n_{e,s}$ (or equivalently, of r_0) can be made from the limiting condition for surface wave driven discharges [72]. For 2.45 GHz driving power frequency, the $n_{e,s}$ should be approx. 10^{18} m^{-3} (when accounting for collisions). Schematic illustration of both compound profiles is in figure 13.

It can be argued that also other properties (concave vs convex, (in)equality to zero at a certain distance, etc) of these two
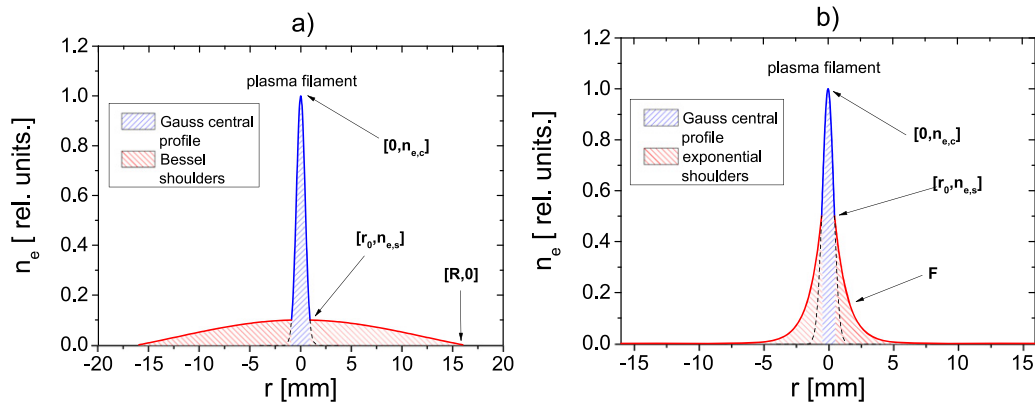
Figure 13. The investigated compound spatial profiles (not to scale) (a) Bessel profile, (b) exponential profile. These profiles are almost independent of the central part (only the stitching point is slightly affected).

functions effectively make them quite distant in the class of permitted profile functions. Therefore, while we are aware of our self-inflicted choice, most conclusions valid for both of these functions should be relevant for other reasonable candidate functions, including the real (albeit unknown) profile.

Finally, the sets of computationally predicted phase shifts for these two compound profiles are plotted in figure 14. There, the half-width of the central filament profile (possible main source of non-linearity) was fixed at 0.35 mm, while different values of $n_{e,c}$ were tried. For the Bessel profile, the values $R = 16$ mm and $R = 77.5$ mm correspond to the distance of waveguides from centre and reactor radius, respectively.

Following observations can be made: (i) computed phase shifts both qualitatively and quantitatively match the experimentally observed phase shifts, (ii) the central maximum $n_{e,c}$ influence is noticeable only for the smallest phase shifts (confirming predictions made in section 5.2), (iii) the phase dependence is almost perfectly linear in $n_{e,s}$, F and R parameters (giving a solid chance to interpolate and extrapolate these data as needed) and (iv) for quite different shoulder profiles, the results are almost comparable. Therefore, as a more general result, one may conclude that the model C gives good results, the central over-critical filament plays a negligible role despite non-zero skin depth and the actual interferometry takes place in spatial profile shoulders, but the exact choice of shoulder profile is not essential. The insensitivity to shoulder profiles can also be interpreted as that from the microwave interferometry point of view—the true measure of the electron presence being not their exact spatial profile but the integral amount of electrons in the cross-section.

There are two more practical points of this final model C to discuss—a potential azimuthal anisotropy of the spatial profile and a possible influence of experimentally induced geometrical errors.

By default, the computed profiles were considered azimuthally isotropic, despite the presence of the metallic waveguides, where the increased surface recombination could result in anisotropy. Fortunately, in most cases, the electron concentration at the waveguide openings is negligible compared to that in the rest of the modelled domain. The exception being the wider Bessel profile ($R = 77.5$ mm

taken as the full reactor radius). There, the zero of the Bessel profile along the microwave beam should be at the distance of waveguides from centre (16 mm), while in the perpendicular direction, the zero of the profile would occur much farther, at the reactor wall (77.5 mm)—for reference, see figure 3. Modelling has shown that results for such anisotropic profile are almost identical to the isotropic case with zero at 16 mm, and therefore are not listed separately.

Obviously, some mechanical and physical imperfections of the experimental procedure can never be avoided altogether. It is, therefore, important to evaluate the typical cases, e.g. waveguide misalignment due to loose parts of the set-up or plasma filament bending slightly away from the axis, etc. The possibility of such mishaps is the reason why monitoring snapshots of the critical region (plasma and waveguides) were acquired during each measurement run, theoretically permitting us to numerically compensate *ex post* for such unwanted movements. Fortunately, however, the computations show that these common alignment errors are not critical for the output phase (error under approx. 15%).

5.4. Microwave torch study results

The experimental part of this paper has two equally important purposes. Firstly, to determine the electron concentration in plasma torch and its dependence on ethanol abundance during plasma chemical synthesis of graphene. Secondly, to test suitability of numerically enhanced microwave interferometry method for this type of plasma (forming an over-critical filament at atmospheric pressure). In both these tasks, the Stark broadening of H_β was used, too. However, it was found (as discussed above) that Stark broadening is not concurrent but a complementary method. The spectroscopy is more suitable for active dense filament, while the interferometry detects lower electron concentration in the dark surrounding region.

As the main experimental parameters, the microwave power and ethanol admixture (diluted by auxiliary Ar, see section 3) flow rate was selected. In figure 15, the estimation of electron concentration $n_{e,c}$ from H_β Stark broadening is shown for various ethanol admixtures at constant microwave power. Naturally, the OES gives greater weight to more luminous parts, effectively measuring the active, bright filament only. One can
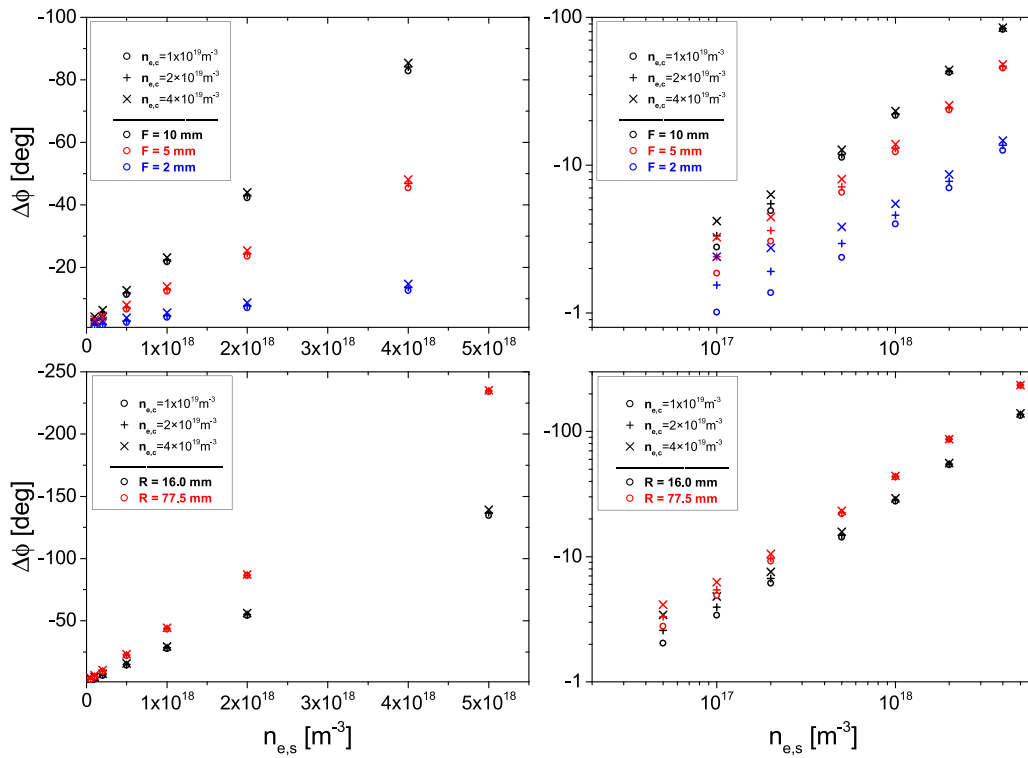
Figure 14. The pre-calculated phase shifts for different Bessel and exponential shoulder profile parameters (left—linear scale; right—log/log scale).
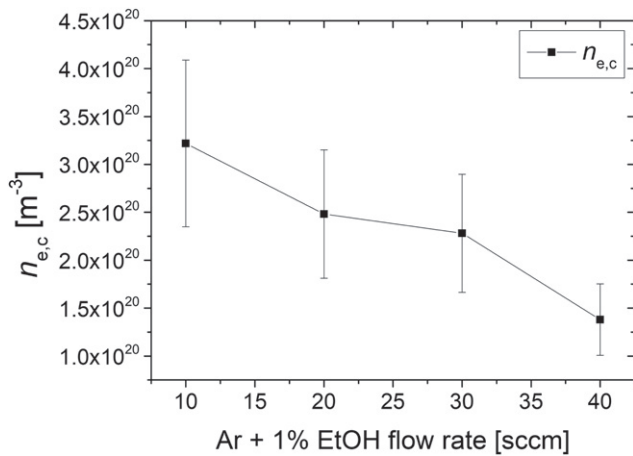

Figure 15. Influence of admixture (Ar + 1% EtOH) on central electron density determined from H_β Stark broadening (axial position 9 mm from the nozzle, central gas flow 700 sccm Ar, excitation power 40 W).

observe that a higher amount of molecular admixture decreases the electron concentration due to heightened energy losses by excitation and dissociation of the precursor molecule and its fragments.

Related to it is a change of the filament length. The current hypothesis [73] is that such discharges operate in surface wave driven mode, i.e. the excitation microwave power guides itself along the plasma/ambient boundary, gradually transferring its energy into the plasma. The net result is rather long and narrow plasma filament with electron density linearly

decreasing with the axial position. The highest electron density is in the wave launching area close to the nozzle tip and the lowest is at the discharge end—the tip of the filament. The surface wave sustaining condition strongly links the plasma length and the microwave excitation power. On a more fundamental level, increased losses due to inelastic electron collisions with molecules (Ar has first excitation level at approx. 11.5 eV) decrease the available power, decreasing the ionisation rate, electron concentration and, by consequence, also the plasma column length.

Actually, the electron density axial profile as calculated from H_β Stark broadening, shown in figure 16, is not linear. It can be explained by the existence of non-linearities and losses by space radiation near the wave launching area (i.e. close to the nozzle). Although this deviation from classical simplified surface wave description is well known, it was recently revisited [73] and is currently under intensive research. Overlapping curves at larger axial distances suggest that amount of ethanol admixture (max 0.1% of total gas flow) does not substantially impact the electron density.

The results above are values inside the active plasma filament. The microwave interferometry can provide the values of electron density in the dark filament surrounding. The single interferometric measurement consists of manually conducted two-step data acquisition (with and without reference arm), performed within a few seconds by careful adjustment of the attenuator knob. Moreover, the experiment was operated in a switch-on/switch-off regime in order to eliminate the effects of gradual heating of waveguide walls (as they expand, the propagation constant inside the waveguide decreases and
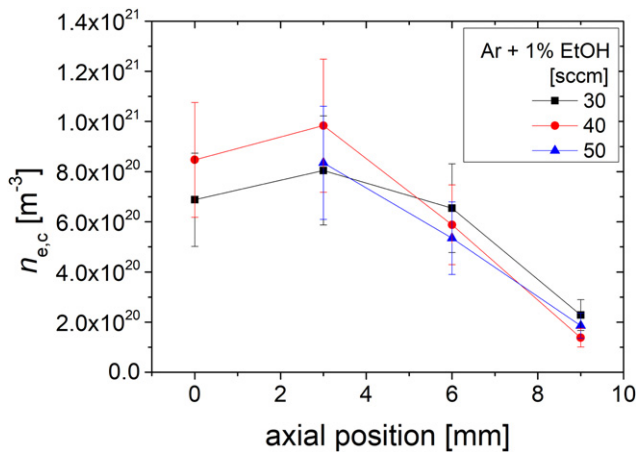
Figure 16. Axial profiles of central electron density in plasma filament, as calculated from H_β Stark broadening. Zero position corresponds to tip of the nozzle. The curves were measured for three Ar + 1% EtOH flow rates (excitation discharge power 40 W, central gas flow 700 sccm Ar).

phantom phase shifts could occur). Despite being subtle, this effect may add up over a long section of the (thermally conducting) waveguide. It forces us to carry out the interferometry while repeatedly switching the discharge on and off for each experimental setting.

Interestingly, the heating of the waveguides can serve as a validation factor for the measured phase shift sign. During the interferometer set-up and initial adjusting, the correct operation of a variable attenuator is easy to observe on the detector signal. However, with a variable phase shifter, it is not obvious, whether a positive or negative phase shift is being introduced (of course, there is a micrometre dial, but still its operation is error-prone). As the waveguide walls cool down after the plasma measurement, the waveguide walls contract and the phase velocity inside increases (leading to negative phase shift over time). On the contrary, if plasma density is in the expected negative phase shift region (as calculated in figure 14), switching off the plasma must yield a positive phase shift, opposite to that of cooling walls. Indeed, this was observed in the experiment, further confirming the results of the numerical model.

The raw phase shifts from microwave interferometry are shown in figure 17. These values have been compared to precalculated numerical results, giving stitching point electron density $n_{e,s}$ as shown in figure 18 for different experimental conditions (excitation power, ethanol admixture). The precalculations obviously depend on the choice of *a priori* unknown spatial profile (stitching point, type of shoulder function, its parameter, etc.)

Although results of all studied spatial profiles are shown in figure 18, some of them (depicted in red) are somewhat arguable: (i) the reactor wide ($R = 77.5$ mm) Bessel profile has problematic boundary condition (as already discussed in the paragraph concerning anisotropy in 5.3), as substantial recombination should occur already at the conductive

waveguide openings. (ii) The fits of steeply decreasing exponential profile ($F = 2$ mm) to measured phase shifts yield values of $n_{e,s}$ often well over 10^{18} m^{-3}. This is higher than one would expect from knowledge that exciting frequency is 2.45 GHz with corresponding electron density of surface wave excited plasma around 1×10^{18} m^{-3} (with collisions, $\nu_m = 5 \times 10^{10}$ s^{-1}). Intuitively, the stitching point should coincide with this threshold.

Unfortunately the price paid for indirectness of the method plus having too many free (and pseudofree) parameters is apparent. The uncertainty of the results stem from three main components: (i) experimental error of interferometric phase shift, including short term noise, long term drift and possible imbalance between diodes and their calibrations. We estimate this error to be around $\pm 0.7°$ for single phase measurement, meaning the error from (two part) phase shift measurement should be approx. $\pm 1°$. This fixed value has obviously larger relative effect when the measured phase shift is small. (ii) Geometry errors. Possible lateral shifts, tilting, curving of the filament. Typically, the error should be below $\pm 15\%$, according to modelling. (iii) Unknown electron density profile. Trying various profiles (shapes, central part electron density, stitching value, radius of main bulk) we arrived at mean error around $\pm 30\%$ of the $n_{e,s}$ value (as can be roughly seen from the spread of respective black datapoints in figure 18). The error bars shown in graph are our estimation of the combined effect of causes (i)–(iii).

While this error hides possible trends, by comparing with figure 13 one can clearly see, that electron densities as high as $n_e > 10^{17}$ m^{-3} extend well into the dark region around the plasma filament.

As discussed before, the total number of electrons seems to be a more dependable parameter than their spatial distribution. Integrating the dark region electron densities from figure 18 over the r, ϕ-plane results in figure 19. Here, the agreement for this total linear electron density (electrons per unit length cylindrical slice) among possible compound profiles is even better.

As the choice of actual profile plays a lesser role, the error due to cause (iii) gets smaller, around $\pm 15\%$. Still, the statistical spread is too large to reveal any definite trend in figure 19. It should be noted, that figure 15 depicting Stark broadening data does not provide any such trend, either. Again, the mean values around $(6 \pm 2) \times 10^{13}$ m^{-1} seem to be quite reliable.

In the bigger picture, results of all of these tested profiles support two main outcomes: (i) the concentration of free electrons in the outer filament region is in the order of 10^{17} m^{-3} for this type of plasma and, at least in the studied range, rather independent of the amount of admixture and discharge excitation power. These values are approximately 2–3 orders of magnitude lower than the electron concentration in active plasma. (ii) The results confirm that extent of these residual electrons is most likely significant (approximately 1 cm away from filament the values in higher order of 10^{16} m^{-3} still can be found) suggesting that volume recombination is not as dominant as one might expect outside the active plasma filament.
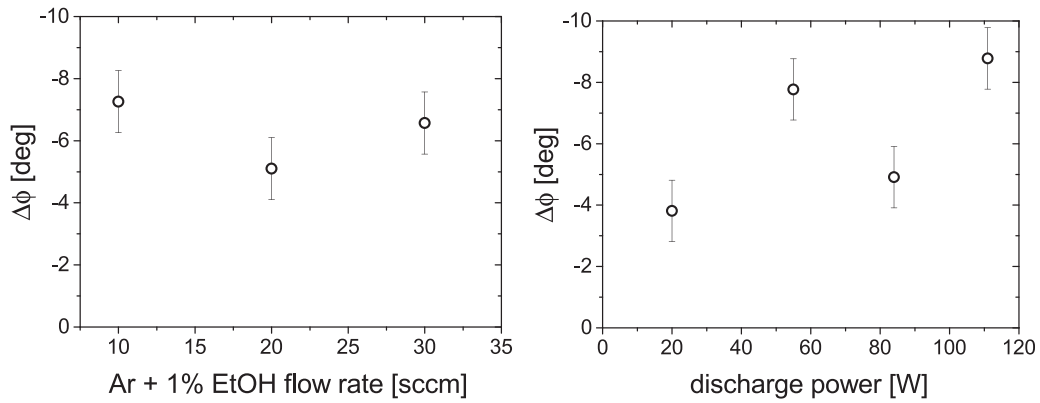
Figure 17. The raw measured phase shifts for varying ethanol admixture flow rate (left, constant discharge excitation power 35 W) and varying excitation power (right, constant Ar + 1% EtOH flow rate 10 sccm) for axial position 15 mm from the nozzle and central gas flow 700 sccm Ar. The experimental error bars estimate of $\pm 1°$ correspond to subtracting two measured phases, each with $0.7°$ uncertainty.
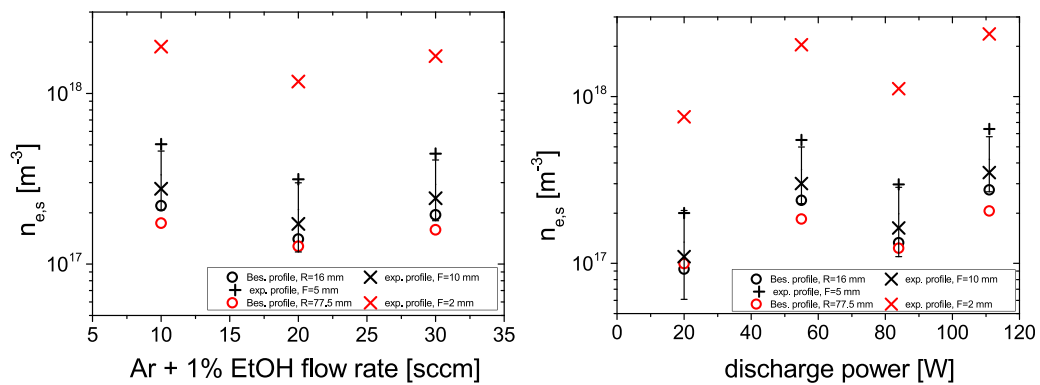

Figure 18. The shoulder stitching electron concentration $n_{e,s}$ from fitting of microwave interferometry data. Red symbols mark less trustworthy values, see text.
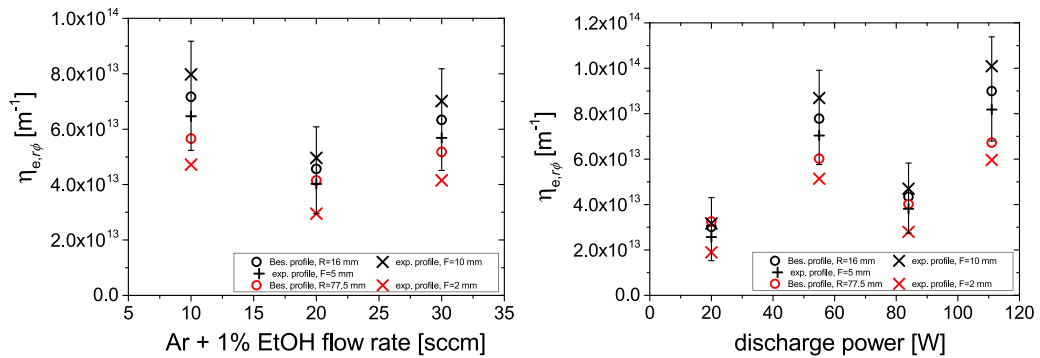

Figure 19. The electron density from the preceding figure integrated over $r\phi$-plane (i.e. $\eta_{e,r\phi}$ is the total number of electrons outside the central part of plasma filament in a unit length cylindrical slice).

6. Conclusions

The use of microwave interferometry for measurement of the electron concentration in the non-luminous surroundings of the atmospheric plasma jets was successfully demonstrated. As many (if not most) classical assumptions of plasma interferometry were intentionally broken, the experimental phase shifts had to be combined with EM numerical model and reference OES measurements in the central active filament. It

was confirmed that main contributions to the observed phase shift are the strong but spatially limited scattering at the over-critical filament boundary and the gradual but spatially extended propagation in sub-critical surroundings.

The paper discusses the importance of radial plasma density profile, both in the active filament itself and its non-luminous surroundings. As the profile was unknown and experimentally inaccessible, a class parametric study was carried out. It was found that the choice of the shoulder function

(profile in the dark surroundings) shape was not exceedingly critical.

Therefore the microwave interferometry can be used as complementary method to Stark broadening, giving consistent values in the non-luminous surroundings of the active filament. With plasma density 2–3 orders of magnitude lower than in active plasma but with a volume of 2–3 orders higher, the contribution of the dark surroundings to overall plasma chemistry can be substantial.

Acknowledgments

ORCID iDs

J Faltýnek ⬤ https://orcid.org/0000-0002-8621-3351
V Kudrle ⬤ https://orcid.org/0000-0002-7669-1691
M Šnírer ⬤ https://orcid.org/0000-0003-0534-5262
J Toman ⬤ https://orcid.org/0000-0002-8391-8073
O Jašek ⬤ https://orcid.org/0000-0002-1416-794X

References

[1] Sharp B L, Chenery S, Jowitt R, Sparkes S T and Fisher A 1994 Spectrom *J. Anal. At.* **9** 171R–188R
[2] Czylkowski D, Hrycak B, Miotk R, Jasiński M, Dors M and Mizeraczyk J 2015 *Eur. Phys. J. Appl. Phys.* **40** 40
[3] Škoro N, Puač N, Živković S, Krstić-Milošević D, Cvelbar U, Malović G and Petrović Z L 2018 *Eur. Phys. J. D* **72** 2
[4] Jašek O, Eliáš M, Zajíčková L, Kučerová Z, Matějková J, Rek A and Buršík J 2007 *J. Phys. Chem. Solids* **68** 738–43
[5] Synek P, Jašek O and Zajíčková L 2014 *Plasma Chem. Plasma Process.* **34** 327341
[6] Toman J, Jašek O Šnírer M, Kudrle V and Jurmanová J 2019 *J. Phys. D: Appl. Phys.* **52** 265205
[7] Tatarová E, Henriques J, Luhrs C C, Dias A, Phillips J, Abrashev M V and Ferreira C M 2013 *Appl. Phys. Lett.* **103** 134101
[8] Dato A 2019 *J. Mater. Res.* **34** 214–30
[9] Tsyganov D *et al* 2020 *Phys. Chem. Chem. Phys.* **22** 4772–87
[10] Rincón R, Muñoz J, Sáez M and Calzada M D 2013 *Spectrochim. Acta B: At. Spectrosc.* **81** 26–35
[11] Prevosto L, Kelly H and Mancinelli B R 2012 *J. Appl. Phys.* **112** 063302
[12] Narishige S, Suzuki S, Bowden M D, Uchino K, Muraoka K, Sakoda T and Park W Z 2000 *Japan. J. Appl. Phys.* **39** 6732
[13] Hubner S, Sousa J S, van der Mullen J and Graham W G 2015 *Plasma Sources Sci. Technol.* **24** 054005
[14] Nedanovska E, Nersisyan G, Morgan T J, Hüwel L, Murakami T, Lewis C L S, Riley D and Graham W G 2015 *J. Appl. Phys.* **117** 013302
[15] Schaub S C, Hummelt J S, Guss W C, Shapiro M A and Temkin R J 2016 *Phys. Plasmas* **23** 083512
[16] Nikiforov A Y, Leys C, Gonzalez M A and Walsh J L 2015 *Plasma Sources Sci. Technol.* **24** 034001
[17] Qi B, Huang J, Gao L and Qiu Y 2009 *Phys. Plasmas* **16** 083301
[18] Kirichenko A Y and Suvorova O A 1998 *Proceedings of the 3rd International Symposium Physics and Engineering of Millimeter and Submillimeter Waves* vol 2 (Kharkov) p 742
[19] van Gessel A F H, Carbone E A D, Bruggeman P J and van der Mullen J J A M 2012 *Plasma Sources Sci. Technol.* **21** 015003
[20] Heald M A and Wharton C B 1965 *Plasma Diagnostics with Microwaves* (New York: Wiley)
[21] Button K J and Wolfe S M 1977 *Proceedings Volume 0105 Far Infrared/Submillimeter Wave: Technology/Applications*
[22] Nakayama K, Tomimoto M, Okajima S, Kawahata K, Tanaka K, Tokuzawa T, Akiyama T and Ito Y 2007 *Plasma Fusion Res.* **2** S1114
[23] Lawyer K A 2016 *Master Thesis* University of Northern British Columbia
[24] Baker D R and Lee S T 1978 *Rev. Sci. Instrum.* **49** 919–22
[25] Olejníček J, Hubička Z, Virostko P, Churpita A and Jastrabík L 2007 *Plasma Process. Polym.* **4** S1022–5
[26] Baeva M, Andrasch M, Ehlbeck J, Loffhagen D and Weltmann K-D 2014 *J. Appl. Phys.* **115** 143301
[27] Cardoso R P, Belmonte T, Noël C, Kosior F and Henrion G 2009 *J. Appl. Phys.* **105** 093306
[28] Li J, Xu Y, Zhang T, Tang J, Wang Y, Zhao W and Duan Y 2017 *J. Appl. Phys.* **122** 013301
[29] Schaefer J, Sigeneger F Šperka J, Rodenburg C and Foest R 2018 *Plasma Phys. Control. Fusion* **60** 014038
[30] Álvarez R, Quintero M C and Rodero A 2004 *Spectrochim. Acta B: At. Spectrosc.* **59** 709–21
[31] Obrusník A, Synek P, Hübner S, van der Mullen J J A M, Zajíčková L and Nijdam S 2016 *Plasma Sources Sci. Technol.* **25** 055018
[32] Siusko Y V and Kovtun Y V 2019 *J. Phys.: Conf. Ser.* **1197** 012001
[33] Jašek O, Toman J, Jurmanová J, Šnírer M, Kudrle V and Buršíková V 2020 *Diam. Relat. Mater.* **105** 107798
[34] Faltýnek J, Hnilica J and Kudrle V 2017 *Plasma Sci. Sources and Technol.* **26** 015010
[35] Yubero C, Calzada M D and Garcia M C 2005 *J. Phys. Soc. Japan* **74** 2249–54
[36] Synek P, Obrusník A, Hübner S, Nijdam S and Zajíčková L 2015 *Plasma Sources Sci. Technol.* **24** 025030
[37] Palomares J M, Hübner S, Carbone E A D, De Vries N, Van Veldhuizen E M, Sola A, Gamero A and van der Mullen J J A M 2012 *Spectrochim. Acta B: At. Spectrosc.* **73** 39–47
[38] Gigosos M A, González M Á and Cardeñoso V 2003 *Spectrochim. Acta B: At. Spectrosc.* **58** 1489–504
[39] Torres J, Palomares J M, Sola A, van der Mullen J J A M and Gamero A 2007 *J. Phys. D: Appl. Phys.* **40** 5929–36
[40] Carbone E, D'Isa F, Hecimovic A and Fantz U 2020 *Plasma Sources Sci. Technol.* **29** 055003
[41] Kunze H J 2009 *Introduction to Plasma Spectroscopy* vol 56 (Berlin: Springer)
[42] Hanson R K, Spearrin R M and Goldenstein C S 2016 *Spectroscopy and Optical Diagnostics for Gases* vol 1 (Switzerland: Springer)
[43] Pozar D M 2011 *Microwave Engineering* 4th edn (New York: Wiley)
[44] Faltýnek J 2014 *Master Thesis* Masaryk University
[45] Lieberman M A and Lichtenberg A J 1994 *Principles of Plasma Discharges and Materials Processing* (New York: Wiley)
[46] Moisan M and Pelletier J 2012 *Physics of Collisional Plasmas* (Berlin: Springer)
[47] Leins M, Walker M, Schulz A, Schumacher U and Stroth U 2012 *Contrib. Plasma Phys.* **52** 615–28
[48] Benova E, Atanasova M, Marinova P, Marchev V and Petrova T B 2013 *Conference 31st ICPIG PS2-056*
[49] Bodrov S, Bukin V, Tsarev M, Murzanev A, Garnov S, Aleksandrov N and Stepanov A 2011 *Opt. Express* **19** 6829–35
[50] Deng B H *et al* 2018 *Rev. Sci. Instrum.* **89** 10B109

[51] Mie G 1908 *Ann. Phys.* **330** 377−445

[52] Zajíčková L, Eliáš M, Jašek O, Kudrle V, Frgala Z, Matějková J, Buršík J and Kadlečíková M 2005 *Plasma Phys. Control. Fusion* **47** B655−66

[53] Ricard A, St-Onge L, Malvos H, Gicquel A, Hubert J and Moisan M 1995 *J. Phys. III* **5** 1269−85

[54] Leipold F, Stark R H, El-Habachi A and Schoenbach K H 2000 *J. Phys. D: Appl. Phys.* **33** 2268

[55] Choi J-Y, Takano N, Urabe K and Tachibana K 2009 *Plasma Sources Sci. Technol.* **18** 035013

[56] Urabe K, Sakai O and Tachibana K 2011 *J. Phys. D: Appl. Phys.* **44** 115203

[57] Nowakowska H, Zakrzewski Z and Moisan M 2001 *J. Phys. D: Appl. Phys.* **34** 1474

[58] Qiuping Z, Cheng C and Yuedong M 2009 *Plasma Sci. Technol.* **11** 560

[59] Christova M, Castaños-Martinez E, Calzada M D, Kabouzi Y, Luque J M and Moisan M 2004 *Appl. Spectrosc.* **58** 1032−7

[60] Kabouzi Y, Calzada M D, Moisan M, Tran K C and Trassy C 2002 *J. Appl. Phys.* **91** 1008−19

[61] Voráč J, Kusýn L and Synek P 2019 *Rev. Sci. Instrum.* **90** 123102

[62] Voráč J, Synek P, Potočňáková L, Hnilica J and Kudrle V 2017 *Plasma Sources Sci. Technol.* **26** 025010

[63] Voráč J, Synek P, Procházka V and Hoder T 2017 *J. Phys. D: Appl. Phys.* **50** 294002

[64] Griem H R 1974 *Spectral Line Broadening by Plasmas* (New York: Academic)

[65] Gigosos M A and Cardeñoso V 1996 *J. Phys. B: At. Mol. Opt. Phys.* **29** 4795

[66] Olchawa W, Olchawa R and Grabowski B 2004 *Eur. Phys. J.* D **28** 119−24

[67] Šperka J 2017 *Dissertation Thesis* Masaryk University

[68] Stepanenko A A, Lee W and Krasheninnikov S I 2017 *Nucl. Mater. Energy* **12** 887−92

[69] Fukunari M, Tanaka S, Shinbayashi R, Yamaguchi Y, Tatematsu Y and Saito T 2019 *Sci. Rep.* **9** 17972

[70] Di Donato L and Sorbello G 2019 *IEEE Trans. Plasma Sci.* **47** 1781−7

[71] Kubečka MŠnírer M, Obrusník A, Kudrle V and Bonaventura Z 2020 *Plasma Sources Sci. Technol.* **29** 075001

[72] Zakrzewski Z, Moisan M and Sauvé G 1993 *Microw. Disch. NATO ASI Ser.* **302** 117−40

[73] Moisan M and Nowakowska H 2018 *Plasma Sources Sci. Technol.* **27** 073001